Frequency-Dependent Streaming Potentials

Philip M. Reppert,*,1 Frank Dale Morgan, David P. Lesmes,† and Laurence Jouniaux‡

*Earth Resources Laboratory, Department of Earth Atmospheric and Planetary Sciences, Massachusetts Institute of Technology, E34-356a, 42 Carleton Street, Cambridge, Massachusetts 02142; †Department of Geology and Geophysics, Boston College, Chestnut Hill, Massachusetts 02167; and ‡Laboratoire de Géologie, URA1316, Ecole Normale Supérieure, 24 Rue Lhamond, 75231 Paris Cedex 05, France

An experimental apparatus and data acquisition system was constructed to measure the streaming potential coupling coefficients as a function of frequency. The purpose of the experiments was to measure, for the first time, the real and imaginary portion of streaming potentials. In addition, the measured frequency range was extended beyond any previous measurements. Frequency-dependent streaming potential experiments were conducted on one glass capillary and two porous glass filters. The sample pore diameters ranged from 1 mm to 34 μm. Two frequency-dependent models (Packard and Pride) were compared to the data. Both Pride's and Packard's models have a good fit to the experimental data in the low- and intermediate-frequency regime. In the high-frequency regime, the data fit the theory after being corrected for capacitance effects of the experimental setup. Pride's generalized model appears to have the ability to more accurately estimate pore sizes in the porous medium samples. Packard's model has one unknown model parameter while Pride's model has four unknown model parameters, two of which can be independently determined experimentally. Pride's additional parameters may allow for a determination of permeability. © 2001 Academic Press

Key Words: **electrokinetic; streaming potential; dynamic; frequency; ac.**

INTRODUCTION

The phenomenon of streaming potentials has been studied for many years. This has led to applications in such diverse fields as chemistry, biology, and geophysics (1–5). The overwhelming majority of this work has been in the area of dc streaming potentials, while very little work has been done in the area of frequency-dependent streaming potentials. Past theoretical and experimental work dealing with the frequency response of streaming potentials has dealt with single-frequency, low-frequency, and frequency response measurements. Single-frequency streaming potential measurements are made at one frequency while varying the pressure in order to get plots of streaming potentials versus pressure without using a flow-through apparatus (6). Low-frequency measurements are used to

extrapolate the frequency-dependent streaming potential value to the dc limit. This is done for the purposes of determining the zeta or surface potentials (7, 8). Low-frequency measurements are also used to determine the effective pore size and hydraulic permeability (9). Frequency-response measurements examine the frequency-dependent behavior of streaming potentials (10, 11). Packard (10) proposed a frequency-dependent streaming potential theory for capillaries where the streaming potential coupling coefficient remains constant at its dc value until the critical frequency is approached by the sinusoidal driving force. At frequencies higher than the critical frequency, the streaming potential coupling coefficient decays with increasing frequency. Packard's experiments were performed on a limited number of capillary samples of large radii (2.083–0.589 mm) and with no changes in solution chemistry. Packard was able to achieve a maximum measuring frequency of 200 Hz. Cooke (11) attempted to duplicate Packard's work, but with limited success; he could not match his capillary data to the theoretical curves of Packard. Cooke's data for porous glass filters appears to have the expected trend predicted by Packard's theory. On closer examination, however, Packard's theory cannot be satisfactorily fitted to Cooke's data. No one to date has satisfactorily fitted frequency-dependent streaming potential data to theoretical curves for porous media of any pore diameter or for capillaries with diameters less than 155 μm.

In 1994, Pride (12) proposed a generalized theory for frequency-dependent streaming potentials in porous media. This theory relates the transport properties and pore-geometry parameters to the samples' streaming potential frequency-response behavior. No experimental work has been performed to validate Pride's theory.

The understanding of frequency-dependent streaming potentials is vital to Earth scientists who study the electromagnetic signals generated by seismic/acoustic waves propagating in the earth. Earth scientists believe that these electromagnetic signals are generated by oscillatory fluid flow in rocks relative to the mineral matrix (13). This relative flow induces a streaming current, which oscillates as an electric dipole at the same frequency as the seismic/acoustic wave exciting the medium. This frequency-dependent streaming current has a countercurrent that flows through the conductive part of the rock (bulk fluid) to develop a frequency-dependent streaming potential.

1 To whom correspondence should be addressed. Present address: Department of Geological Sciences, 338 Brackett Hall, Clemson University, Clemson, SC, 29634. Fax: (864) 656-1041. E-mail: reppert@clemson.edu.

Frequency-dependent streaming potentials induced by a seismic wave are often referred to as the seismoelectric effect (14, 15). Some Earth scientists believe that the streaming potential frequency response may be useful in determining *in situ* permeability (16, 17).

In this paper, the real and imaginary streaming potential frequency response for a capillary is developed based on Packard's model, which is then compared to Pride's model. Then a discussion of the experimental system and methodology is provided. This is followed by a presentation of the first data where the complex frequency response for one glass capillary and two porous glass filters is presented. These experiments cover a frequency range of 1–500 Hz.

DC STREAMING POTENTIALS

Streaming potentials are a subset of electrokinetic phenomena, which includes electroosmosis, electrophoresis, and sedimentation potentials. Electrokinetic phenomena are a consequence of a mobile space charge region that exists at the interfacial boundary of two different phases. This region is commonly referred to as the electrical double layer (EDL). The most simplified approximations of the EDL can be represented by a parallel-plate capacitor (Helmholtz model) or a charge distribution that decays exponentially away from the surface, Gouy–Chapman model (18). A more accurate model takes into account the finite size of ions by combining the Helmholtz and Gouy–Chapman models where a fixed layer exists at the surface (Stern layer) and a diffuse layer extends from the fixed layer into the bulk solution (Gouy–Chapman diffuse layer). This model is often referred to as the Stern model of the electrical double layer. More specifically the interfacial region, shown schematically in Fig. 1, consists of the inner Helmholtz plane (IH) where ions are adsorbed to the surface and the outer Helmholtz plane (OH) where ions are rigidly held by electrostatic forces and cannot move. The closest plane to the surface at which fluid motion can take place is called the slipping plane. The slipping plane has a potential defined as the zeta potential (ζ), which is a characteristic of the solid and liquid that constitute the interface. The diffuse layer extends from the OH into the bulk of the liquid phase. The distance at which the diffuse layer potential (ψ_0) has been reduced to ψ_0/e is referred to as the Debye length. This is often used as a measure of how far the diffuse layer extends into the bulk fluid.

Streaming potentials occur when relative motion between the two phases displaces ions tangentially along the slipping plane by viscous effects in the liquid. This displacement of ions generates a convection current (I_{conv}) and has properties similar to an ideal current source. For a capillary, I_{conv} is defined by

$$I_{\text{conv}}(r) = \int v(r)\rho_c(r)\,dr, \qquad [1]$$

in which $v(r)$ is the fluid particle velocity, dr is an infinitesimal part of the cross section, and $\rho_c(r)$ is the charge distribution
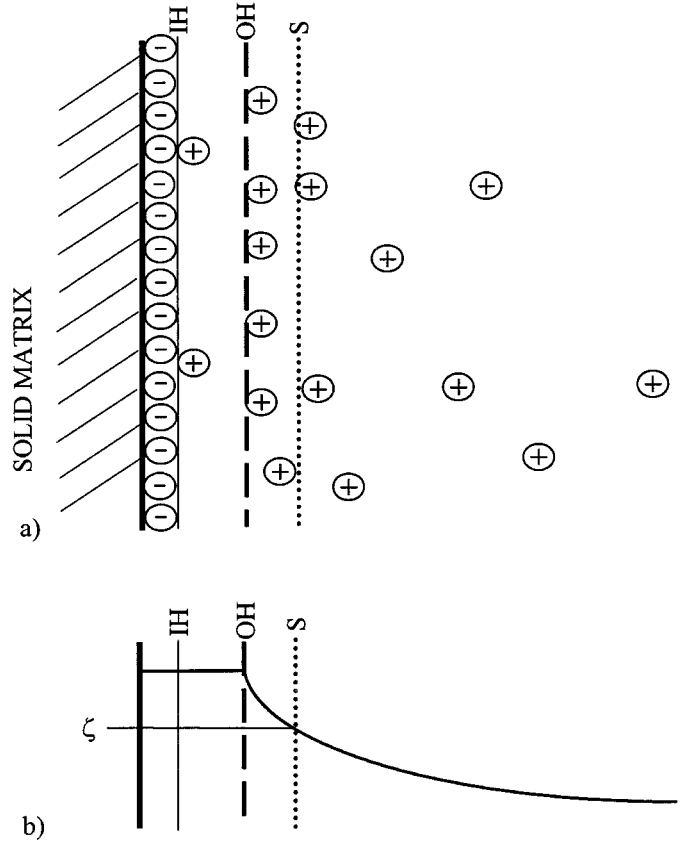

FIG. 1. (a) The Stern model of the electrical double layer. (b) One of the possible potential distributions of the Stern model. This model assumes that in the Stern layer the potential varies linearly.

in the capillary. The solution to this integral can be found in a variety of texts and is given by

$$I_{\text{conv}}(r) = \frac{\pi \varepsilon a^2 \zeta \Delta P}{\eta l}, \qquad [2]$$

where ε is the permittivity of the fluid, a is the radius of the capillary, l is the length of the capillary, ΔP is the pressure across the sample, η is the viscosity of the fluid, and ζ is the zeta potential.

In steady-state equilibrium the convection current must be balanced by a conduction current (I_{cond}) (18). Hence by ohms law,

$$I_{\text{cond}}(r) = \frac{\pi \sigma a^2}{l}\Delta V, \qquad [3]$$

where σ is the fluid conductivity and ΔV is the voltage measured across the sample. Equating the convection and conduction currents, which must be equal at equilibrium, leads to the Helmholtz–Smoluchowski equation (18)

$$\Delta V = \frac{\varepsilon \zeta}{\eta \sigma}\Delta P. \qquad [4]$$

It should be noted when viewing Eq. [4] that it does not include geometry terms for the specimen. The ratio $\Delta V / \Delta P$ is referred to as the cross-coupling coefficient or simply the coupling coefficient in the rest of the paper. When the capillary or pore-space thickness approach the dimensions of the diffuse layer (0.1 μm for 0.001 M solution), surface effects must be considered (2, 4). The radii of the samples used in our experiments are much larger than the Debye length; hence, these effects are not be addressed.

AC STREAMING POTENTIALS

The basic principles of ac streaming potentials are presented following the methodology of Packard (10). To better understand the physics of ac streaming potentials, appropriate comparisons are made to the frequency-dependent hydraulic problem previously solved by others (19).

The basic electrokinetic principles of dc and ac streaming potentials are the same. The difference is in the hydrodynamic part of the solution where the constant pressure of the dc case is replaced by a sinusoidal pressure in the ac case. Therefore, the starting point for the derivation must go back to the hydrodynamic problem where the Navier–Stokes equation,

$$\rho \frac{\partial \bar{v}(r, \omega)}{\partial t} \exp(-i\omega t)$$
$$= -\nabla P(\omega) \exp(-i\omega t) + \eta \nabla^2 \bar{v}(r, \omega) \exp(-i\omega t), \quad [5]$$

is shown with a sinusoidal driving pressure applied across the sample. Equation [5] can be rearranged into the form

$$\left[\frac{\partial^2}{\partial r^2} + \frac{1}{r} \frac{\partial}{\partial r} + k^2 \right] v(r, \omega) = \frac{\Delta P(\omega)}{\eta l}, \quad [6]$$

where the gradient of the pressure has been replaced by $\Delta P(\omega)/l$ and

$$k^2 = \frac{-i\omega \rho}{\eta}. \quad [7]$$

It is apparent that the solution can be expressed using Bessel functions, with the general solution to Eq. [6] expressed as

$$\bar{v}(r, \omega) = -\frac{\Delta P(\omega)}{k^2 l \eta} + C_1 J_0(kr) + C_2 Y_0(kr). \quad [8]$$

The applied boundary conditions are $v(r, \omega) = 0$, when $r = a$; $v(r, \omega) = $ finite, when $r = 0$, and also noting $Y_0(0) = \infty$, which then requires that $C_2 = 0$. This leads to

$$C_1 = -\frac{\Delta P(\omega)}{\eta l k^2} \frac{1}{J_0(ka)}. \quad [9]$$

Substituting Eq. [9] into Eq. [8] gives

$$\bar{v}(r, \omega) = \frac{\Delta P(\omega)}{\eta l k^2} \left[\frac{J_0(kr)}{J_0(ka)} - 1 \right] \quad [10]$$

as the frequency-dependent velocity inside a capillary. Integrating Eq. [10] over the cross-sectional area of the capillary gives

$$v(\omega) = \frac{\Delta P(\omega)}{\eta l k^2} \left[\frac{2}{ka} \frac{J_1(ka)}{J_0(ka)} - 1 \right] \quad [11]$$

as the average fluid velocity inside a capillary, which is the frequency-dependent hydraulic solution for a capillary.

Now that the frequency-dependent fluid flow inside a capillary has been presented, Eq. [10] can be substituted into Eq. [1] to give

$$I_{\text{conv}}(\omega) = \int 2\pi r \rho_c(r) \bar{v}(r, \omega) \, dr, \quad [12]$$

which is the frequency-dependent convection current inside a capillary, where the charge density in the capillary in cylindrical coordinates is given by

$$\rho_c(r) = -\varepsilon \nabla^2 \psi_0(r) = -\frac{\varepsilon}{r} \frac{\partial}{\partial r} \left(r \frac{\partial \psi_0(r)}{\partial r} \right). \quad [13]$$

Integrating Eq. [12] from the center of the capillary to the slipping plane under the assumption that the capillary radius is large compared to the Debye length of the EDL (10, 12) gives

$$I_{\text{conv}}(\omega) = -\frac{2\pi \varepsilon a \zeta}{\eta l k} \frac{\Delta P(\omega)}{J_0(ka)} \frac{J_1(ka)}{J_0(ka)} \quad [14]$$

as the frequency-dependent convection current for a capillary.

As in the DC case, at equilibrium, the convection current must be balanced by a conduction current. The conduction current is determined using Ohm's law, where the conduction current is given by

$$I_{\text{cond}}(\omega) = \Delta V(\omega) \pi a^2 \frac{\sigma}{l}. \quad [15]$$

Setting the convection current equal to the conduction current gives

$$C(\omega) = \frac{\Delta V(\omega)}{\Delta P(\omega)} = \left[\frac{\varepsilon \zeta}{\sigma \eta} \right] \frac{-2}{ka} \frac{J_1(ka)}{J_0(ka)}. \quad [16]$$

This is the ac Helmholtz–Smoluchowski equation in a form similar to that presented by Packard (10), where $C(\omega)$ is the frequency-dependent cross-coupling coefficient. The ac Helmhotz–Smoluchowski equation reduces to the dc form in the limit as ω goes to zero, which can be demonstrated using Bessel function recursive relations or by taking the low-frequency approximation of Eq. [16]. Figure 2 shows the real and imaginary
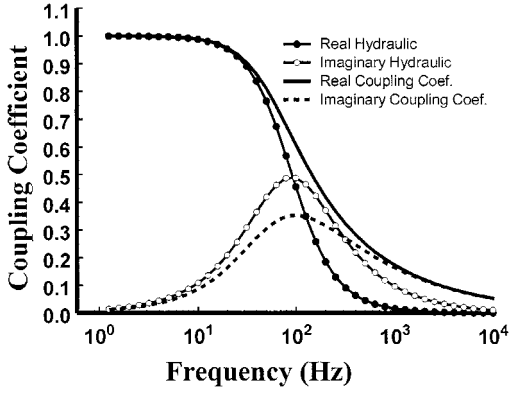
FIG. 2. Theoretical comparison of the frequency-dependent hydraulic solution, Eq. [11] and the frequency-dependent streaming potential solution. The real and imaginary portions of both solutions are shown. The coupling coefficients are normalized.

portions of the ac coupling coefficient, Eq. [16], and a plot of the frequency-dependent hydraulic equation, Eq. [11]. Figure 3 shows the phase part of Eqs. [11] and [16]. It can be seen in these two figures that the general behavior of the two equations is similar. In particular, the low-frequency behavior is identical but the high-frequency behavior diverges as one goes to higher frequencies.

At first examination of frequency-dependent streaming potentials and frequency-dependent hydraulics, it might be expected that the two phenomena would have identical behavior, since the frequency-dependent streaming potential behavior is governed by the frequency-dependent fluid flow. The different responses of the ac Helmholtz–Smoluchowski equation, Eq. [16], and the frequency-dependent hydraulic equation, Eq. [11], are easier to understand by looking at the series and asymptotic approximations for the low- and high-frequency cases, respectively. Following the methodology of Crandall (20) (which was developed for the acoustic case), the low-frequency and high-frequency approximations are made. The two separate equations are then combined to form a single equation.
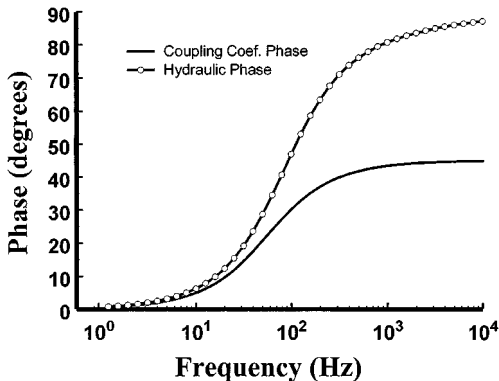

FIG. 3. Phase comparison of the frequency-dependent coupling coefficients and frequency-dependent hydraulics, where the phase is $0°$ for both curves at 0 Hz.

Starting with the ac Helmholtz–Smoluchowski expression, Eq. [16], and substituting the low-frequency approximations of the Bessel functions (20) J_0 and J_1, with

$$J_0(x) = \sum_{n=0}^{\infty} \frac{(-1/4x^2)^k}{k!\Gamma(n+1)} \qquad [17]$$

and

$$J_1(x) = \frac{x}{2} \sum_{n=0}^{\infty} \frac{(-1/4x^2)^k}{k!\Gamma(n+2)}, \qquad [18]$$

where x represents ka and ka < 1. Substituting these two approximations into Eq. [16] and taking the Lim $n \to \infty$ gives

$$\frac{\Delta V(\omega)}{\Delta P(\omega)} = \lim_{n\to\infty}\left[\frac{\varepsilon\zeta}{\sigma\eta}\right]\left[\frac{2}{ka}\left\{\frac{\frac{x}{2}\sum_{n=0}^{\infty}\frac{(-1/4x^2)^k}{k!\Gamma(n+2)}}{\sum_{n=0}^{\infty}\frac{(-1/4x^2)^k}{k!\Gamma(n+1)}}\right\}\right]$$

$$= \left[\frac{\varepsilon\zeta}{\sigma\eta}\right]\left[\frac{2}{ka}\frac{x}{2}\right]. \qquad [19]$$

Since $x = $ ka, the low-frequency approximation reduces to

$$\underset{ka<1}{C}(\omega) = \frac{\Delta V(\omega)}{\Delta P[\omega]} = \left[\frac{\varepsilon\zeta}{\sigma\eta}\right] = \frac{\Delta V}{\Delta P}. \qquad [20]$$

The high-frequency approximation used for the Bessel functions J_0 and J_1 are given by

$$\frac{J_1(x\sqrt{-i})}{J_0(x\sqrt{-i})} = -i, \qquad [21]$$

which can be found in Crandall (20) or which can be easily proven using the asymptotic approximations of Abramowitz and Stegun (21). In Eq. [16],

$$ka = a\sqrt{-\frac{i\rho\omega}{\eta}}, \qquad [22]$$

from which the following substitution is made in Eq. [22]:

$$x\sqrt{-i} = a\sqrt{-\frac{i\rho\omega}{\eta}} = a\sqrt{\frac{\rho\omega}{\eta}}\sqrt{-i}. \qquad [23]$$

Then substituting Eq. [21] and Eq. [23] into Eq. [16] gives

$$\underset{ka>10}{C}(\omega) = \left[\frac{\varepsilon\zeta}{\sigma\eta}\right]\left[\frac{-2i}{ka}\right] = \left[\frac{\varepsilon\zeta}{\sigma\eta}\right]\left[\frac{-2i}{a\sqrt{\frac{-i\rho\omega}{\eta}}}\right]. \qquad [24]$$
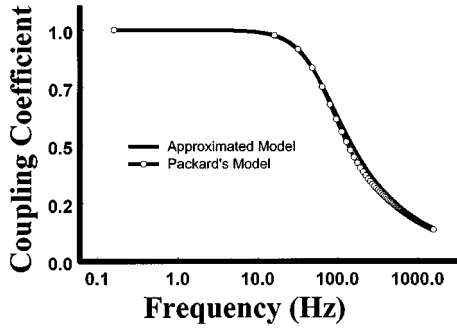
FIG. 4. Normalized comparison of the Bessel function solution, Eq. [16], to the approximated Bessel function solution, Eq. [26].

Equation [24] can then be modified to

$$\underset{ka>10}{C(\omega)} = \left[\frac{\varepsilon\zeta}{\sigma\eta}\right]\left[\frac{-2}{a}\sqrt{\frac{\eta}{\omega\rho}}\left(\frac{1}{\sqrt{2}} - \frac{1}{\sqrt{2}}i\right)\right]. \qquad [25]$$

Combining the low-frequency and high-frequency approximations gives

$$\text{CA}(\omega) = \left[\frac{\varepsilon\zeta}{\sigma\eta}\right]\left[1 - \frac{2}{a}\sqrt{\frac{\eta}{\omega\rho}}\left(\frac{1}{\sqrt{2}} - \frac{1}{\sqrt{2}}i\right)\right], \qquad [26]$$

where $\text{CA}(\omega)$ represents the approximated cross-coupling coefficient. In Fig. 4, the solution using Bessel function approximations, Eq. [26], is plotted against the Bessel function solution of Eq. [16]. It can be seen in Fig. 4 that the two solutions are nearly identical. There is a slight divergence in the intermediate-frequency range, $1 > ka > 10$, which was not accounted for in the approximation. However, the error is smaller than measurements can detect.

It can be seen in Eq. [26] and Figs. 2, 3, and 4 that as the frequency is increased inertial effects start to retard the motion of the fluid within the pore space. This occurs as the fluid makes a transition from viscous dominated flow to inertial dominated flow. At the higher frequencies the flow becomes inefficient, requiring more energy to move the same amount of liquid the same distance. Therefore at frequencies higher than the transition from viscous to inertial flow, more pressure is required to shear the same quantity of ions from the diffuse zone than when strictly in the viscous flow regime. It can also be seen in Eq. [26] and Fig. 2 that at higher frequencies the real and imaginary parts of the coupling coefficient solution are decreasing at the same rate. This explains the 45° phase angle found at high frequencies in Fig. 3.

One might ask why the frequency-dependent hydraulics and frequency-dependent streaming potentials do not have the same behavior. By comparing the form of the frequency-dependent streaming potential (FSP) approximate solution to the frequency-dependent hydraulic (FDH) solution, valuable insight into the physics that causes the difference in behavior between FDH and FSP solutions can be obtained. This comparison is made using Eqs. [20], [25], and [26] of the FSP approximation and Eq. [11] of the (FDH) solution. The low-frequency approximation to Eq. [11] is (20)

$$\underset{ka<1}{H(\omega)} = \left(\frac{8}{a^2} + \frac{4}{3}i\rho\omega\right)^{-1}, \qquad [27]$$

where $H(\omega)$ represents the frequency-dependent hydraulic solution. When $ka < 1$, the real term in Eq. [27] dominates over the imaginary term. This implies that at low frequencies the flow is real (no vorticity present) and as the frequency is increased an inertial component starts to develop in the flow (vorticity present). However, when $ka < 1$ the inertial term remains insignificant and the flow is essentially viscous. Therefore, both low-frequency FDH and FSP solution approximations approach the dc limit at low frequencies.

The high-frequency approximation of the FDH equation is given by (20)

$$\underset{ka>10}{H(\omega)} = \left(i\rho\omega + \frac{1}{r}2\eta\sqrt{\frac{\rho\omega}{2\eta}}(1+i)\right)^{-1}, \qquad [28]$$

where $(2\eta/\rho\omega)^{1/2}$ is the viscous skin depth. When examining Eq. [28], it can be seen that the bulk of the fluid is governed by the imaginary terms and thus inertial flow exists. However, when the viscous skin depth is sufficiently small, a second-order effect starts to dominate and the imaginary term starts to decrease at the same rate as the real term, giving rise to a diminished propagation velocity. It becomes apparent from the approximation analysis that the high-frequency solution causes the difference between the frequency-dependent hydraulics and the frequency-dependent streaming potential behavior. When the integral of Eq. [12] is evaluated, most of the contribution to the integral occurs along the wall of the capillary where most of the charge distribution is located. This region near the wall is also where the second-order effect of the hydraulic solution starts to dominate. Consequently, the frequency-dependent streaming potential exhibits high-frequency behavior that follows the form of the second-order effect of the hydraulic solution.

AC STREAMING POTENTIALS IN POROUS MEDIA

A model for ac streaming potentials in a porous medium derived from first principles was developed by Pride (12). Pride's version of the ac Helmholtz–Smoluchowski equation is given by

$$\text{CP}(\omega) = \frac{\Delta V(\omega)}{\Delta P(\omega)}$$

$$= \left[\frac{\varepsilon\zeta}{\eta\sigma}\right]\left[1 - i\frac{\omega}{\omega_t}\frac{m}{4}\left(1 - 2\frac{d}{\Lambda}\right)^2\left(1 - i^{\frac{3}{2}}d\sqrt{\frac{\omega\rho}{\eta}}\right)^2\right]^{-\frac{1}{2}}, \qquad [29]$$

where CP(ω) represents the AC coupling coefficient for porous media using Pride's model, d is the Debye length, and Λ is a typical pore radius representing a weighted volume-to-surface ratio (19). The transition frequency

$$\omega_t \equiv \frac{\phi}{\alpha_\infty k_0} \frac{\eta}{\rho}, \qquad [30]$$

as defined by Pride (12), separates the low-frequency viscous flow regime from the high-frequency inertial flow regime. In Fig. 2 the transition frequency occurs where the hydraulic imaginary curve intercepts the hydraulic real curve. Porosity is given by ϕ tortuosity by α_∞, and the dc permeability by k_0. The dimensionless number m is defined as

$$m \equiv \frac{\phi}{\alpha_\infty k_0} \Lambda^2, \qquad [31]$$

which is also a function of the pore microgeometry, which reduces to 8 for a capillary. Closer examination of the ac porous media coupling coefficient, Eq. [29], reveals that to a first-order approximation the response is determined by the transition frequency ω_t and the dc coupling coefficient.

Figure 5 shows the normalized real and imaginary parts of the theoretical ac coupling for three capillaries of different radius using Eq. [16]. The obvious characteristic of the curves is that the transition frequency shifts with changing radius of the capillary. This relationship is easily evident when looking at the equation for the transition frequency, Eq. [30], and realizing that the dc permeability for a capillary is

$$k_0 = \frac{a^2}{8}. \qquad [32]$$

The transition frequency for capillary then becomes

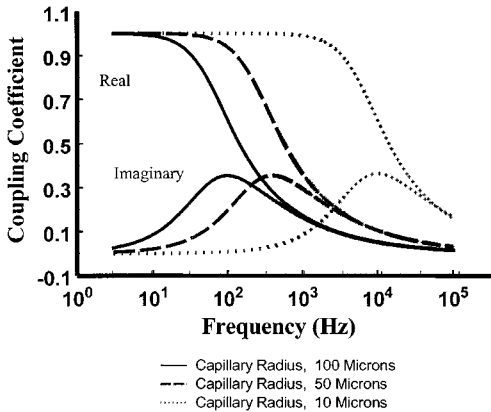$$\omega_t(\text{cap}) = \frac{8}{a^2} \frac{\eta}{\rho}. \qquad [33]$$

FIG. 5. Normalized coupling coefficient of the real and imaginary components for three capillaries of different radii.

COMPARISON OF PACKARD'S AND PRIDE'S MODELS

Pride (12) generated his model by creating low-frequency and high-frequency models separately and then combining them into a single combined model. Equations [34] and [35] show Pride's low-frequency and high-frequency models, respectively, when capillary geometry terms are used and second-order effects are neglected. Capillary geometry terms imply that $m = 8$, $\phi = 1$, $\alpha_\infty = 1$, $\Lambda = a$, and $k_0 = (a^2)/8$, where a is the capillary radius. Second-order effects occur when the Debye length is large compared to the capillary radius:

$$CP_{LAC} = \frac{\varepsilon \zeta}{\eta \sigma} \qquad [34]$$

$$CP_{HAC} = -2 \left[\frac{\varepsilon \zeta}{\eta \sigma} \right] \frac{i^{\frac{1}{2}} \delta}{\Lambda}. \qquad [35]$$

Equation [35] can be rewritten as

$$CP_{HAC} = \left[\frac{\varepsilon \zeta}{\eta \sigma} \right] \left[\frac{-2}{a} \sqrt{\frac{\eta}{\rho \omega}} \sqrt{i} \right], \qquad [36]$$

where δ is the viscous skin depth and is given by $(2\eta/\rho\omega)^{1/2}$. Equation [36] can also be rewritten as

$$CP_{HAC} = \left[\frac{\varepsilon \zeta}{\eta \sigma} \right] \left[\frac{-2}{a} \sqrt{\frac{\eta}{\rho \omega}} \left(\frac{1}{\sqrt{2}} - \frac{1}{\sqrt{2}} i \right) \right], \qquad [37]$$

which clearly shows that the real and imaginary parts of the high-frequency solution are identical to Eq. [25] in the Bessel function approximation. One possibility of combining the low-frequency and high-frequency solutions into a single model is

$$CP(\omega) = \left[\frac{\varepsilon \zeta}{\eta \sigma} \right] \left[1 - \frac{2}{a} \sqrt{\frac{\eta}{\omega \rho}} \left(\frac{1}{\sqrt{2}} - \frac{1}{\sqrt{2}} i \right) \right], \qquad [38]$$

where capillary geometry is used and second order-effects are neglected.

The simplified version of Pride's model, Eq. [38], as opposed to the full equation, is compared to Packard's equation for two reasons. First, the second-order effects do not affect the model within the range of frequency or concentrations for which Pride's model is defined. Second, the simplified model of Pride, Eq. [38], is identical to the approximated form the Packard's model, Eq. [26]. This implies, when using capillary geometry terms and neglecting second-order effects, that Pride's model is identical to Packard's model when the series and asymptotic approximations are used.

A visual comparison of Packard's and Pride's models can be made by looking at Fig. 4, where Eqs. [16] and [38] are compared. A slight discrepancy between the two curves becomes apparent, which is addressed earlier in this paper. To completely approximate the Bessel function, the range where ka is greater than one but less than 10 must be addressed. Packard addresses

this range because the Bessel function form inherently covers the whole range. It appears from the comparison of Packard's Bessel function form to Pride's model that Pride's model does not completely address this region. When Fig. 4 is compared to actual measurements, however, it is difficult to resolve the difference between the two curves when experimental error is accounted for in the data. Consequently, Pride's model is adequate in this region.

EXPERIMENTAL APPROACH

The approach used to collect the streaming potential data was to hold the capillary or porous filter stationary and oscillate the fluid back and forth through the sample using a sinusoidal driving pressure at one end while having the other end open to the atmosphere. Silver silver–chloride electrodes were placed on either side of the sample in fluid ports to keep them out of the fluid flow path (22). The frequency response of the electrodes was measured using a four-electrode method and found to be flat in the region used in this experiment. The electrode measurements were also verified through the use of a capacitive coupled antenna placed around the outside of the sample. The pressure was monitored on the high-pressure and atmospheric-pressure sides of the sample by miniature hydrophones that have a flat frequency response from 1 to 20 kHz. The acrylic apparatus, which holds the sample, electrodes, and hydrophones, is shown schematically in Fig. 6. The enclosure around the sample and preamplifiers is constructed of Mu-metal. Mu-metal is used because of its superior electromagnetic shielding properties. The acrylic housing that holds the sample is additionally enclosed in an aluminum housing, and the electromechanical shaker that produces the driving pressure is enclosed in a separate steel box. This large quantity of shielding is required for two reasons. The first is that the laboratory is an electrically noisy environment. The second is that the pressure source is being generated by an electromechanical transducer, which is driven at the same frequency as the measured streaming potential. The driving transducer and associated leads emit enough electromagnetic signal (EMF) at the same frequency being measured to sometimes affect the measured results. Depending on the pore or capillary diameters, the resistance of the sample could be several hundred
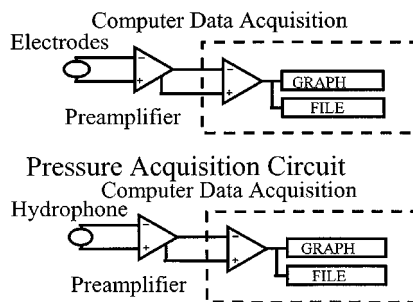
FIG. 7. A simplified representation of the streaming potential data acquisition circuit is shown. A Labview 12-bit AD board was used to acquire the data in the computer.

megaohms, which causes the sample to act as an antenna for the EMF fields produced by the electromechanical transducer. The acrylic housing has 50 kg of lead placed on it to reduce any sample vibration.

The waveforms were sampled using two instrument preamplifiers and a 12-bit analog-to-digital board with 24.8-μV resolution. Electrometers or FET preamplifiers were required as input buffers due to the high impedance of the samples (.5 MΩ to 1 GΩ). A schematic representation of the data acquisition system is shown in Fig. 7. The data were analyzed using spectral analysis with a Hanning window applied to the data prior to spectral analysis. In addition to spectral analysis, the time-domain voltage and pressure were monitored at each driving frequency. The raw data were saved for possible future processing. Cross-correlation analysis of the signals was also performed as a verification of the amplitude spectrum measurements.

DATA/RESULTS

To test Packard's and Pride's models experimentally, the pore diameters of the samples must be known. The pore diameter is used as an adjustable parameter in the models to fit the theory to the data. Actual pore diameters are then compared to the experimentally determined pore diameters. The pore diameters of the glass samples were provided by the manufacturer.

The glass samples consist of a capillary and two porous filters. Capillary 1 has an inner diameter that ranges from 0.8 to 1.1 mm, and a length of 60 cm. Porous Filter A has manufacturer-determined pore diameters ranging from 145 to 175 μm, an overall diameter of 1 cm, and a thickness of 2 mm. Porous Filter B has manufacturer-determined pore diameters ranging from 70 to 100 μm, an overall diameter of 1.9 cm, and a thickness of 1 cm.

The experiments were carried out using 10^{-3} and $10^{-3.7}$ M KCl with a pH of 5.5. Assuming a concentration of 10^{-4} M KCl, the Debye length was found to be much less than the radius of the pore space. Therefore, second-order effects can be neglected in Pride's model.

Figure 8 shows the measurements of the coupling coefficient versus frequency for Capillary 1 along with a theoretical curve
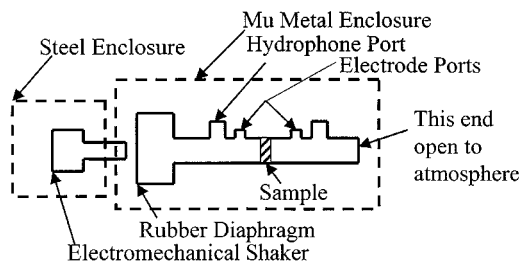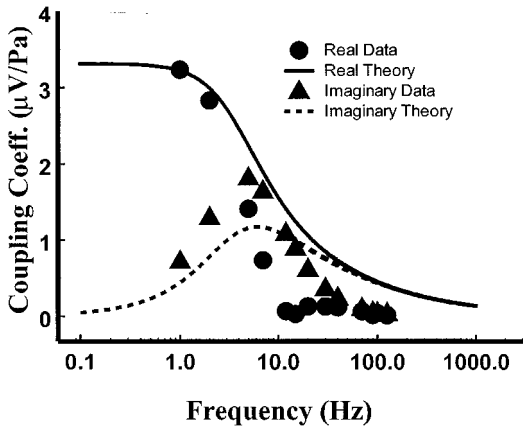

FIG. 6. A simplified schematic representation of the test cell and pressure source. The apparatus is constructed of Plexiglas and bolted to a heavy metal plate.

FIG. 8. Cross-coupling real and imaginary uncorrected data for Capillary 1 plotted along with the theory for a 0.8-mm capillary.

FIG. 10. Corrected cross-coupling real and imaginary data for 60-mm-long, 0.8-mm-diameter capillary plotted along with the theory for a 0.8-mm capillary. Error bars are not shown because they fall within the size of the data points.

for Eq. [26]. It can be seen that the data do not have a satisfactory fit to the theory. In addition to the streaming potential data of Fig. 8, the frequency-dependent impedance of the sample and measuring circuit was also determined and is shown in Fig. 9. The impedance of the sample and measuring circuit was determined using a four-electrode method. The RC of the circuit was found to have a resistance of 1 GΩ and a capacitance of 25 pF. The resistance was determined to be on the order of the resistance of a 0.8-mm capillary filled with $10^{-3.7}$ M KCl. The capacitance was found to be on the order of the input capacitance of the amplifier and the capacitance of the wire leads. The data in Fig. 8 were then corrected for this impedance by normalizing the real and imaginary portions of the impedance at the particular frequencies of the streaming potential measurement. This normalized impedance was then divided into the data. The corrected data are shown in Fig. 10, where a good correlation between the theory and the data is evident. At the higher frequencies, signal-to-noise problems caused the fit to have a little more scatter. The transition frequency determined from the fit of the theoretical curve is 7.1 Hz, which gives a capillary diameter
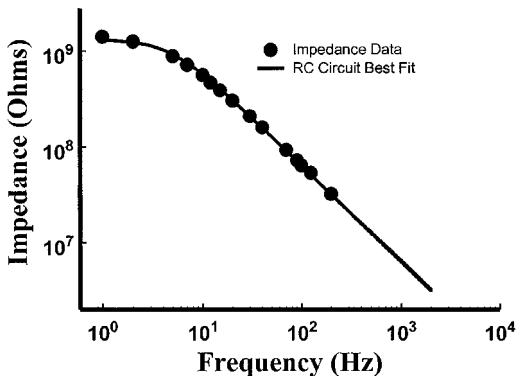
of 0.8 mm. This is in agreement with the manufacturer-provided diameter of 0.8–1.1 mm for this type of capillary. Looking at Fig. 10, it can be seen that for the higher frequencies, inertial flow essentially dominates in Capillary 1.

The corrected data for Porous Filter A, shown in Fig. 11, are plotted against Eq. [26]. As can be seen, the theory fits the data well. Fitting the theoretical curve to the data for Porous Filter A gives a pore radius of 65 μm and a transition frequency of 269 Hz. The manufacture-provided pore radii for the Porous Filter A are 72.5–87 mm.

Figure 12 shows the corrected data for Porous Filter B along with the best-fit theoretical curve. Porous filter B has its best fit to Pride's theory, Eq. [26], using a 40-μm pore radius and a transition frequency of 710 Hz. Recall that the pore radii provided by the manufacturer for Porous Filter B are 35 to 50 μm. The data for Porous Filter B fits the theory very well in the low-frequency and the intermediate-frequency regions. At the higher frequencies, there is a little more scatter than at the low frequencies due to poor signal-to-noise ratio.

FIG. 9. Capillary 1 impedance data plotted with the best RC circuit response. The resistance and capacitance of the RC circuit are 1 GΩ and 25 pF, respectively.
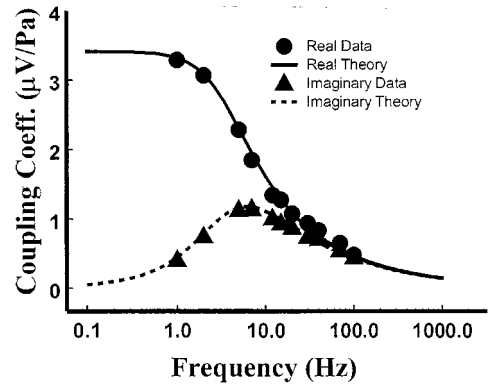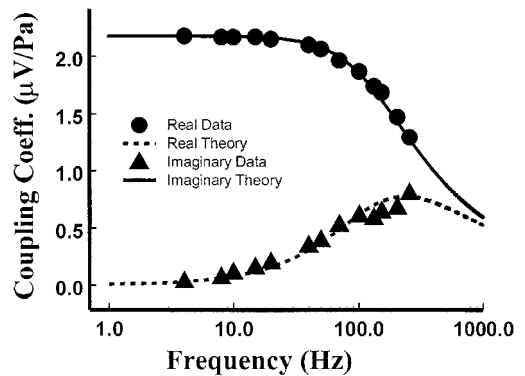

FIG. 11. Porous Filter A corrected cross-coupling real and imaginary data plotted with the theoretical response. The transition frequency was determined to be 269 Hz, which gives a pore radius of 65 μm. The manufacturer provided pore radius for porous filter B ranges from 72.5 to 87 μm. Error bars are not shown because they fall within the size of the data points.
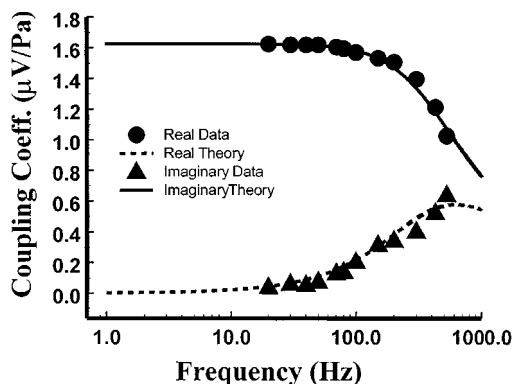
FIG. 12. Porous Filter B corrected cross-coupling frequency response data plotted along with the theoretical response. The transition frequency was determined to be 710 Hz, which gives a pore radius of 40 μm. The manufacturer provided pore radius for porous filter B ranges from 35 to 50 μm. Error bars are not shown because they fall within the size of the data points.

It appears from the data that the experimentally determined pore radii tend toward the low range of radii provided by the manufacturers. This may imply that the frequency-dependent streaming potential response is controlled by the smallest pore geometry in a fluid path. Further research is required to say for certain why the frequency response tends toward the smaller pore sizes. At the present time it appears to be related only to the hydrodynamic portion of the problem.

DISCUSSION AND APPLICATIONS

The emphasis of this study has been to examine, for the first time, complex streaming potentials and to extend the frequency range covered by this type of experiment. As a consequence of this study Packard's and Pride's theories have been verified over a range of pore sizes. Both Packard's and Pride's theories fit the data nearly identically. The transition frequency is the important parameter to be determined uniquely, for both capillaries and porous filters, from frequency-dependent streaming potential curves. From the transition frequency, the pore size can be determined. The transition frequency can be determined graphically from the data or by curve fitting the theory to the data and then determining the transition frequency from the theory. Packard's theory for a capillary is related to the capillary radius and the viscosity and density of the fluid. In Pride's model one additional parameter (m) is included if the second-order parameters are neglected and Λ is taken as the pore radius. The second-order effect parameters are important only where the pore sizes are very small and/or the electrolyte concentration is very low.

The data collected on glass filters with pore diameters much larger than the diffuse zone indicate that the curves generated using Pride's and Packard's theories cannot be distinguished from each other. This result confirms the analysis done earlier in the paper. What is different between the theories is that Pride's model includes second-order effects, which are eliminated in the approximation made during the solution of Eq. [16],

Packard's model. In this respect, Pride's model appears to be more complete and general, but the accuracy in these regions has not been confirmed. From the data thus far collected on porous filters, it can be concluded that the curves generated by Packard's and Pride's models can accurately fit the data. Therefore, both Packard's and Pride's models give identical results when used with realistic frequency ranges and solution chemistries as shown from the theoretical analysis and the experimental data.

SUMMARY/CONCLUSION

Real and imaginary parts of frequency-dependent streaming potentials were measured for the first time. A comparison of streaming potential data to proposed models has been presented for various pore sizes. Although there is a slight discrepancy between the capillary model and the generalized model, overall both Packard's and Pride's models fit the frequency-dependent streaming potential capillary data. For porous media, both Packard's capillary model and Pride's porous media model fit the data, which allows the pore size to be estimated. The difference between the two models comes from the model parameters used to fit the curve. When using Pride's model, if either m or Λ are know a priori, it allows determination of the other parameter. From the results thus far presented, the frequency streaming potential response may be governed by the smallest pore geometry in the fluid path.

Currently plans are underway to extend the frequency range of the experiment to 20–30 kHz. This will allow study of a wider range of samples, including rocks. Studying a broader sampling of rocks will help us to understand the relationship between frequency-dependent streaming potentials and permeability as alluded to by others (16, 17). A set of samples with well-defined geometries will better help to confirm how well the models can predict pore size and whether the response is governed by the pore-throat size. Last, performing frequency-dependent studies at higher temperatures and pressures will help us to ascertain what is happening to the solution chemistry and electrical double layer at *in situ* temperatures and pressures for rocks. This understanding has importance to the oil industry as well as to Earth scientists for the study of earthquake nucleation (23).

REFERENCES

1. Kurtz, R. J., Findl, E., Kurtz, A. B., and Stormo, L. C., *J. Colloid Interface Sci.* **57,** 28–39 (1976).

2. Levine, S., Marriott, J. R., Neale, C., and Epstein, N., *J. Colloid Interface Sci.* **52,** 136–149 (1975).

3. Rice, C. L., and Whitehead, R., *J. Phys. Chem.* **69**(11) (1965).

4. Morgan, F. D., Williams, E. R., and Madden, T. R., *J. Geophys. Res.* **94,** 12,449–12,461 (1989).

5. Ishido, T., and Mizutani, H., *J. Geophy. Res.* **86,** 1763–1775 (1981).

6. Sears, A. R., and Groves, J. N., *J. Colloid Interface Sci.* **65,** 479 (1977).

7. Pengra, D. P., Shi, L., Li, S. X., and Wong, P., "MRS Symposium Proceedings, Boston, December 1995."

8. Wong, P., U.S. Patent 5,417,104 (1995).

9. Li, S. X., Pengra, D. B., and Wong, P., *Phy. Rev. E* **51,** 5748–5751 (1995).

10. Packard, R. G., *J. Chem. Phys.* **21,** 303–307 (1953).

11. Cooke, C. E., *J. Chem. Phys.* **23,** 2299–2303 (1955).

12. Pride, S. R., *Phys. Rev. B.* **50,** 15,678–15,696 (1994).

13. Thompson, A. H., and Gist, G. A., *The Leading Edge*, **December,** 1169 (1993).

14. Haartsen, M. W., and Pride, S. R., *in* "64th Ann. Internat. Mtg. Soc. Expl. Geophys., Expanded Abstracts," pp. 1155–1158, 1994.

15. Zhu, Z., Cheng, C., and Toksöz, M. N., *in* "64th Ann. Internat. Mtg. Soc. Expl. Geophys., Expanded Abstracts," pp. 26–29, 1994.

16. Mikhailov, O. V., Haartsen M. W., and Toksöz, M. N., *Geophysics* **62,** 1–9 (1997).

17. Reppert, P. M., and Morgan, F. D., *in* "Transactions of the 99th Annual Meeting of the American Geophysists Union," T32H-04, 1998.

18. Overbeek, J. Th., *in* "Irreversible Systems" (H. R. Kruyt, Eds.), Vol. 1. Elsevier, New York, 1952.

19. Johnson, D. L., Koplik, J., and Schwartz, L. M., *Phys. Rev. Lett.* **57,** 2564–2567 (1986).

20. Crandall, I. B., "Theory of Vibrating Systems and Sound." Van Norstrand, New York, 1926.

21. Abramowitz, M., and Stegun, I. A., "Handbook of Mathematical Functions With Formula, Graphs, and Mathematical Tables." U.S. National Bureau of Standards, 1964.

22. Morgan, F. D., *in* "Lecture Notes in Earth Sciences" (S. Bhattacharji, G. M. Friedman, H. J. Neugebauer, and A Seilacher, Eds.), Vol. 27, Springer-Verlag, Berlin/New York (1989).

23. Morgan, F. D., *Eos Trans.* AGU, F173 (1995).